

Fiber-integrated phase-change reconfigurable optical attenuator

Cite as: APL Photon. 4, 111301 (2019); doi: 10.1063/1.5116000

Submitted: 20 June 2019 • Accepted: 9 October 2019 •

Published Online: 1 November 2019



View Online



Export Citation



CrossMark

Tiago Martins,^{1,2} Behrad Gholipour,^{1,3,4} Davide Piccinotti,¹ Kevin F. MacDonald,¹  Anna C. Peacock,¹ Orlando Frazão,² and Nikolay I. Zheludev^{1,5}

AFFILIATIONS

¹Optoelectronics Research Centre, University of Southampton, Southampton SO17 1BJ, United Kingdom

²INESC TEC and Department of Physics and Astronomy, Faculty of Sciences, University of Porto, Rua do Campo Alegre, 687, 4150-179 Porto, Portugal

³Department of Chemistry, University of Southampton, Southampton SO17 1BJ, United Kingdom

⁴Department of Electrical and Computer Engineering, University of Alberta, Edmonton, Alberta T6G 1H9, Canada

⁵Centre for Disruptive Photonic Technologies, SPMS & TPI, Nanyang Technological University, 637371, Singapore

ABSTRACT

We report on the experimental demonstration of an optical-fiber-integrated, nonvolatile transmission switching device. The operating mechanism exploits a cavity resonance spectral shift associated with an induced change in the refractive index of a high-index thin film on the polished side facet of the fiber. In the present case, a thermally induced amorphous-crystalline structural transition in a 500 nm layer of germanium antimony telluride at a distance of 500 nm from the core-cladding interface of an SMF-28 single-mode fiber delivers resonant transmission contrast >0.5 dB/mm at 1315 nm. Contrast is a function of active layer proximity to the core, while operating wavelength is determined by layer thickness—varying thickness by a few tens of nanometers can provide for tuning over the entire near-infrared telecoms spectral range.

© 2019 Author(s). All article content, except where otherwise noted, is licensed under a Creative Commons Attribution (CC BY) license (<http://creativecommons.org/licenses/by/4.0/>). <https://doi.org/10.1063/1.5116000>

Optical fibers are among the most mature and widely deployed photonic technology platforms.¹ However, while levels of optical interconnection and integration have increased (even to the on-chip scale), and as advanced quantum optical networks have emerged, all-optical and nonvolatile switching in fiber remains challenging.

In pursuit of such functionalities, desired for the elimination of energy consuming optical-electronic conversions, for “optical memory,” and for the realization of optical neuromorphic computing, recent years have seen growing interest in the development of active, adaptive, tunable, and nonlinear optical fibers.^{2–5} To achieve such active functionalities, fibers typically incorporate materials such as semiconductors,^{6,7} transition metal dichalcogenides,⁸ and metals,^{9,10} which are more traditionally found in planar device architectures. These can be integrated as thin film coatings deposited on the end facets or polished side-walls of step/graded-index fibers or on the internal surface(s) of hollow-core fibers.^{11–13} In the present case,

we employ a side-polished (or “D-shaped”) fiber device geometry, wherein the cladding thickness over a short length of one side of the fiber is reduced such that the evanescent tail of the guided mode outside the core can interact with an external active medium or analyte at (or in the optical near field of) the remnant cladding surface. This configuration, as compared to in-line (end facet) or in-fiber (hollow core) geometries, provides a platform for the realization of transmission-mode devices using standard thin film deposition tools and processes (typically configured for planar substrates), without the need for subsequent assembly (splicing, lens-based input/output coupling, etc.). It also provides straightforward access to the active medium at the point where its interaction with the guided mode in the fiber is strongest, e.g., for attachment of electrodes, exposure to an external illumination source, or contact with a chemical analyte. The extended interaction lengths in this configuration also enable facile tuning of modulation depth/sensitivity in switching/sensing devices.

Here, we hybridize a chalcogenide semiconductor phase-change medium (germanium antimony telluride, as widely used in rewritable optical data storage) with side-polished single-mode silica optical fibers (SMF-28) to realize integrated nonvolatile, high contrast optically reconfigurable attenuators [Fig. 1(a)] that can be engineered by design to operate anywhere within a broad near-infrared spectral range encompassing the telecoms O- to L-bands (from 1260 to 1625 nm).

Chalcogenide semiconductor alloys (of sulfur, selenium, or tellurium covalently bound to “network formers” such as arsenic, germanium, antimony, and gallium) can be prepared in various forms, from microparticles/nanoparticles and optical fibers to vapor-deposited monolayers and thin films.^{14–17} They are noted for providing a variety of compositionally tunable optical properties, including high infrared transparency, strong optical nonlinearity, and photorefractivity.^{18–21} Certain compositions have been identified recently as topological insulators, UV-visible plasmonic, low (subunitary) refractive index, and “low-epsilon” (relative permittivity $\epsilon \sim 0$) media.^{22–29} Chalcogenides are also recognized for their ability to absorb high levels of gaseous, metallic, and rare-earth dopants,^{30–32} but they are perhaps best known (especially commercially, in the context of rewritable data storage) as phase-change media, which can be switched in a nonvolatile fashion between optoelectronically distinct amorphous and crystalline structural phase states.^{33–35} Transitions can be thermally, electrically, or optically induced and can bring about substantive, broadband changes in refractive index on nanosecond to femtosecond time scales.^{36–39} As such, chalcogenides present a uniquely versatile material platform, offering a variety of intriguing (stoichiometrically variable and dynamically switchable/tunable) electromagnetic wave and

light-matter interaction phenomena, which may be exploited for planar and optical fiber-integrated photonic device applications.

In the present study, we utilize germanium antimony telluride ($\text{Ge}_2\text{Sb}_2\text{Te}_5$ or GST) as a near-infrared high-index phase-change medium. Over the 1000–1700 nm wavelength range, the amorphous-to-crystalline transition brings about an increase of $\sim 50\%$ in the near spectrally flat refractive index n . There is an associated increase in extinction coefficient κ , which decreases with increasing wavelength for both phases [Fig. 1(c)]. GST films with a thickness of $t = 500$ nm were deposited on side-polished SMF-28 fibers [Fig. 1(b)], by RF sputtering (Kurt J. Lesker Nano 38): A base pressure of 2×10^{-4} mbar is achieved prior to deposition and high-purity argon is used as the sputtering gas (70 ccpm to strike and 37 ccpm to maintain the plasma). The fibers are held within 10 K of room temperature on a rotating plate 150 mm from the target to produce low-stress amorphous films. The fibers (by Phoenix Photonics Ltd.) each had a nominal side-polished facet of length $l = 5$ mm at a distance d from the core of either 2.4 or 0.5 μm [see Fig. 1(a)], providing, respectively, for weak and strong regimes of interaction between the guided optical mode and the applied coating. (GST is deposited over a length of fiber $> l$ but cannot interact with the guided mode at any point outside the polished section—at full-cladding thickness, $d \sim 58 \mu\text{m}$.)

Near-IR transmission spectra [Figs. 2(a) and 2(b)] were measured using a fiber-coupled broadband light source (Thorlabs SLS201L) and an optical spectrum analyzer (Ando AQ-6315E). Figure 2(a) shows spectra for uncoated side-polished fibers alongside that of an unpolished reference length of the SMF-28 fiber. All three are essentially flat over the 1200–1500 nm wavelength range of interest. As one would expect, the two polished fibers have slightly higher transmission losses than the unpolished fiber, although in the absence of any coating there is relatively little to distinguish between the two core-to-polished-facet distances. The $d = 2.4$ and 0.5 μm fibers, respectively, present average losses over the 1200–1500 nm spectral range (relative to the reference fiber) of 0.37 and 0.48 dB. This picture changes markedly with the introduction of an amorphous GST layer on the polished side facets of the fibers [Fig. 2(b)]. Absolute transmission losses are increased by a few decibels in both side-polished cases because the presence of the high-index film distorts the guided mode. However, while the spectral dispersion of transmission remains flat when the chalcogenide film is located at some distance from the core ($d = 2.4 \mu\text{m}$), a pronounced transmission resonance is seen when it is located in closer proximity ($d = 0.5 \mu\text{m}$). Numerical modeling illustrates how this resonant response is related to the excitation of a Fabry-Pérot mode in the remnant cladding and GST coating layers. The strength of coupling to this mode is a strong function of the core-to-polished-facet distance d [Fig. 2(c)], while the spectral position of the resonance is determined primarily by GST thickness t .

Simulations consider GST-coated sections of side-polished fiber up to 160 μm in length (long enough to accurately reproduce key dependences of device performance on GST film thickness, structural phase state, and proximity to the core and short enough to be computationally tractable with a sufficiently fine 3D mesh density). This analysis employs ellipsometrically measured values for the refractive index and extinction coefficient of GST, as presented in Fig. 1(c), and assumes lossless nondispersive indices of 1.45 and 1.44, respectively, for the fiber core and cladding. It assumes

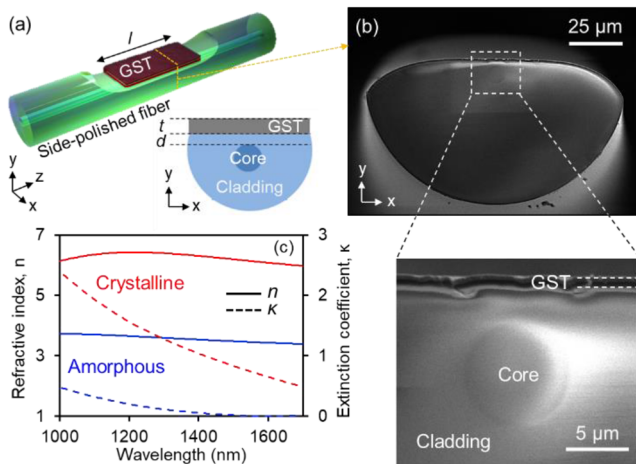


FIG. 1. (a) Dimensional schematics of the phase change reconfigurable optical attenuator. (a) GST-coated side-polished optical fiber. (b) Cross-sectional scanning electron microscope images of such a device, where $d = 2.4 \mu\text{m}$, $t = 500$ nm. (Note that, in practice, GST is deposited over a length of fiber greater than just the polished section, but the coating can only interact with the guided mode over the polished facet length, l .) (c) Spectral dispersion of refractive index n (solid lines) and extinction coefficient κ (dashed) for GST in its amorphous (blue lines) and crystalline (red) phase states.

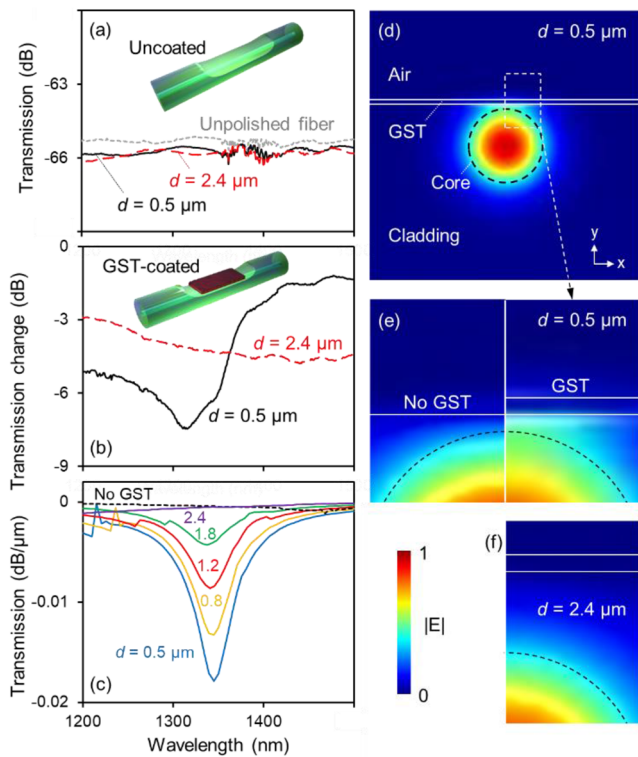


FIG. 2. (a) Experimentally measured transmission spectra for bare, i.e., uncoated, side-polished fibers (core-to-polished-facet distances d as labeled; polished facet length $l = 5$ mm) and a matching length of unpolished fiber. (b) Measured spectral dispersion of the change in transmission resulting from the presence of a $t = 500$ nm amorphous GST layer on the polished facets (each relative to the same fiber's uncoated transmission level). (c) Numerically simulated propagation loss spectra for side-polished fibers with a selection of core-to-polished-facet distances d (as labeled) coated with 500 nm of amorphous GST. Also shown for reference is the spectrum for an uncoated fiber with $d = 0.5 \mu\text{m}$. (d) Numerically simulated cross-sectional distribution of electric field in the xy plane of a fiber with a core-to-polished-facet distance of $0.5 \mu\text{m}$ and 500 nm GST coating thickness, at the 1348 nm resonance wavelength. (e) Detail of the core/remnant cladding/GST coating region for an uncoated fiber (right and left halves, respectively). (f) Corresponding map for a GST-coated fiber with $d = 2.4 \mu\text{m}$.

monochromatic illumination and equal parts of x - and y -polarized light (parallel and perpendicular to the polished facet, respectively). Eigenmode analysis (conducted using Lumerical MODE Solutions) is employed to identify the fundamental mode supported by the device structure for different polish depths. These mode profiles are then used as the input to a finite-difference time domain (FDTD) propagation model from which transmission loss spectra and cross-sectional electric field distributions are derived. There is good agreement between experiment and simulation in regard to the fact that the resonance only emerges when the GST film is located in close proximity to the core (at $d < 2 \mu\text{m}$) and in terms of the resonance wavelength, which is a strong function of GST thickness. Indeed, it is found that the spectral position of the resonance may be tuned over the near-infrared telecommunication range (O- to L-bands, which

extend from 1260 to 1625 nm) by varying GST thickness by only a few tens of nanometers (see [supplementary material](#), Fig. S1). The small ~ 30 nm offset between experimental and simulated resonance spectral positions in [Fig. 2](#) corresponds to a discrepancy in measured or assumed GST thickness or refractive index of $< 3\%$.

Cross-sectional field distributions [[Fig. 2\(e\)](#)] also show that in the absence of GST, the guided mode is essentially unperturbed, i.e., remains confined to the core, even when the cladding is polished to $d = 0.5 \mu\text{m}$. When GST is present on the polished facet, mode confinement to the core is progressively weakened with decreasing d below $\sim 2 \mu\text{m}$. The high-index layer acts as a lossy Fabry-Pérot cavity, in which a standing wave distribution of electric field is established, as shown in the inset of [Fig. 3\(c\)](#) (thereby accounting for the dependence of resonance wavelength on the thickness t). The strength of coupling between this cavity and the guided mode and thus the depth of the transmission resonance are functions of the remnant cladding thickness d . Simulations differ from the experiment in that they assume monochromatic, coherent illumination, and for this reason they predict levels of resonant absorption per unit length (via an interference phenomenon) that are approximately an order of magnitude larger than observed in the experiment (performed with a minimally coherent broadband, tungsten filament, light source). As such, they illustrate levels of performance expected in laser-based (e.g., telecoms) signal processing devices. The quality factor Q of the resonance, being primarily a function of the GST extinction coefficient, does not depend on d .

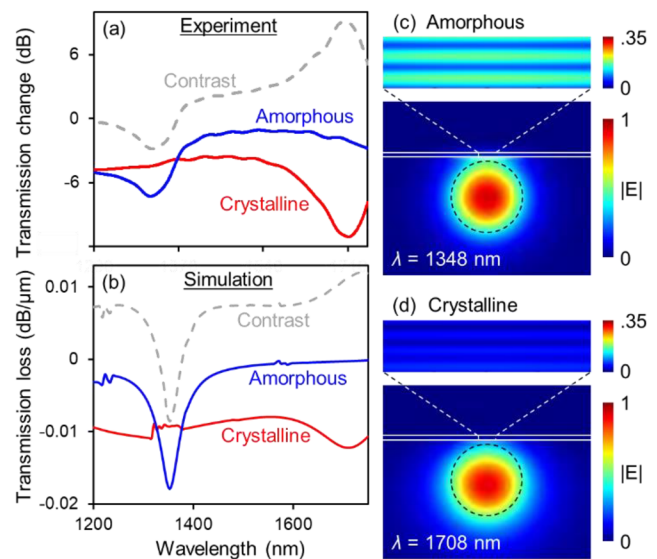


FIG. 3. (a) Experimentally measured and (b) numerically simulated spectral dispersion of propagation loss for a side-polished fiber ($d = 0.5 \mu\text{m}$) coated with GST ($t = 500$ nm) in its amorphous (blue lines) and crystalline (red) states, and the corresponding dispersion of propagation loss contrast, defined as $10 \log(T_{\text{amorphous}}/T_{\text{crystalline}})$ (dashed gray lines). [(c) and (d)] Simulated cross-sectional distributions of normalized electric field in the xy plane, including the expanded detail of the GST layer, for the (c) amorphous and (d) crystalline phase states of GST, at transmission resonance wavelengths of 1348 and 1708 nm, respectively.

The nonvolatile amorphous-to-crystalline transition in chalcogenides is an annealing process initiated by increasing the temperature of the material to a point above its glass-transition temperature T_g ($\sim 160^\circ\text{C}$ for GST) but below its melting point T_m (600°C). In the present case, this is achieved uniformly in the GST film over the whole side-polished fiber facet by holding the fiber at 300°C on a hotplate for 20 min. In device applications, the transition could alternatively be initiated by localized pulsed laser- or electrical current-induced heating, as in optical disc and phase-change RAM data storage technologies. The reverse crystalline-to-amorphous transition is a melt-quenching process requiring local transient heating to a temperature above T_m and rapid cooling. It is not demonstrated as part of the present study as this temperature dynamic cannot be achieved in the GST film by heating/cooling the whole fiber. (In device applications, this transition would again be initiated by pulsed laser- or electronic excitation, with higher pulse energy than for the annealing transition.) Moreover, the GST would need to be encapsulated against deformation and atmospheric degradation at $>T_m$ (e.g., in rewritable optical discs, the phase-change medium is located between protective layers of $\text{ZnS}:\text{SiO}_2$).

Figure 3 shows the effects on side-polished fiber ($d = 0.5\ \mu\text{m}$) transmission of converting the GST coating from its amorphous to its crystalline state, whereby both its refractive index n and extinction coefficient κ increase: The phase transition in GST brings about a red shift of 390 nm in the spectral position of the transmission resonance, with a change in absolute transmission of $-2.8\ \text{dB}$ at the amorphous phase resonance wavelength (1315 nm) and $9.1\ \text{dB}$ at the crystalline phase resonance wavelength (1708 nm)—giving contrast ratios that are in either case sufficient at least for short-reach (intrachip/interchip) optical interconnect applications.⁴⁰ The resonance red shift is accurately reproduced in numerical simulations [Fig. 3(b)], but the model also predicts a reduction in the depth and quality of the resonance upon crystallization—derived from weaker coupling to the Fabry-Perot mode [Figs. 3(c) and 3(d)] in a higher-index, higher-extinction coefficient film, which is not seen in the experiment. Minor discrepancies between experiment and numerical modeling (for both phase states of GST) are attributed to manufacturing imperfections, i.e., deviations from the ideal rectilinear geometry of the model, and defects in the GST film. The mismatch in crystalline phase resonance quality suggests that the extinction coefficient of crystalline GST in the experimental device is lower than is assumed in simulations, which may be accounted for by oxidation and/or stoichiometric changes arising during crystallization.

In summary, we have demonstrated the functional principle of a side-polished optical fiber-integrated phase-change device providing for nonvolatile control of near-infrared guided mode transmission. The amorphous-crystalline phase transition in a thin, high-index chalcogenide film on the side facet of a single-mode fiber modulates optical transmission at resonant operational wavelengths set by design—in the present case, a 500 nm layer of germanium antimony telluride ($\text{Ge}_2\text{Sb}_2\text{Te}_5$ or GST) delivers a maximum transmission contrast of 2.8 dB at 1315 nm and 9.1 dB at 1708 nm. Resonance wavelengths can be set, at the point of device fabrication, anywhere within the transparency range of the chalcogenide and/or supporting fiber by adjusting the thickness of the chalcogenide film. For example, GST thicknesses ranging from 460 to 620 nm would be sufficient to cover a spectral range from 1250 nm (telecoms O-band) to 1590 nm (L-band). Transmission contrast and insertion losses are

functions of the polished facet's proximity to the fiber core and the extinction coefficients of the chalcogenide's amorphous and crystalline phase states. Indeed, the exceptional compositional variety of chalcogenide semiconductor alloys—the stoichiometric tunability of refractive indices, transition temperatures, etc.—offers considerable design flexibility to the present device concept.

Robust devices supporting reversible phase switching over many cycles—i.e., full “optical memory” function whereby data are encoded in/read as the transmission level at the designed resonance (signal) wavelength—may be realized by adding a protective (low-index) dielectric coating to the active domain of GST, thereby encapsulating it in the manner of the functional chalcogenide layers in rewritable optical discs. Structural transitions in GST (in both directions) may be initiated optically by control laser pulses, perhaps delivered through the fiber itself at a wavelength different from the signal: GST absorbs strongly, for example, at shorter visible wavelengths. While a conventionally guided mode in the fiber core would not transfer energy efficiently to the GST film, control pulses could be phase-matched and coupled to a cladding mode using a long-period fiber grating (LPFG).^{41,42} It should be noted that full amorphous-crystalline phase transition is not essential for maximizing optical transmission contrast at the amorphous phase resonance wavelength. As can be seen from Fig. 3, partial crystallization, resulting in a smaller refractive index change and smaller red shift, would suffice to deliver the same transmission attenuation function at lower switching energy (the extent of crystallization being a function of annealing temperature and time).³⁹ We envisage that additional functionality and design freedom may be introduced to such devices by patterning the active layer—a metamaterial structure in an optically switched device may, for example, simultaneously enhance transmission contrast at the signal wavelength and absorption in GST at the control wavelength.

See [supplementary material](#) for additional data on resonance spectral position as a function of GST film thickness.

This work was supported by the Engineering and Physical Sciences Research Council, UK (Grant No. EP/M009122/1); the Singapore Ministry of Education (Grant No. MOE2016-T3-1-006); and Fundação para a Ciência e Tecnologia (Grant No. PD/BD/135008/2017). Following a period of embargo, the data from this paper will be available from the University of Southampton repository: <https://doi.org/10.5258/SOTON/D1121>.

REFERENCES

- ¹D. J. Richardson, *Science* **330**(6002), 327–328 (2010).
- ²B. Gholipour, P. Bastock, C. Craig, K. Khan, D. Hewak, and C. Soci, *Adv. Opt. Mater.* **3**(5), 634 (2015).
- ³J. M. Dudley and J. R. Taylor, *Nat. Photonics* **3**(2), 85–90 (2009).
- ⁴S. Danto, Z. Ruff, Z. Wang, J. D. Joannopoulos, and Y. Fink, *Adv. Funct. Mater.* **21**(6), 1095–1101 (2011).
- ⁵A. F. Abouraddy, M. Bayindir, G. Benoit, S. D. Hart, K. Kuriki, N. Orf, O. Shapira, F. Sorin, B. Temelkuran, and Y. Fink, *Nat. Mater.* **6**(5), 336–347 (2007).
- ⁶R. He, P. J. A. Sazio, A. C. Peacock, N. Healy, J. R. Sparks, M. Krishnamurthi, V. Gopalan, and J. V. Badding, *Nat. Photonics* **6**(3), 174–179 (2012).
- ⁷J. Ballato, T. Hawkins, P. Foy, R. Stolen, B. Kokuoz, M. Ellison, C. McMillen, J. Reppert, A. M. Rao, M. Daw, S. R. Sharma, R. Shori, O. Stafsudd, R. R. Rice, and D. R. Powers, *Opt. Express* **16**(23), 18675 (2008).

- ⁸H. Zhang, N. Healy, A. F. J. Runge, C. C. Huang, D. W. Hewak, and A. C. Peacock, *Opt. Lett.* **43**(13), 3100 (2018).
- ⁹B. Gholipour, P. Bastock, L. Cui, C. Craig, K. Khan, D. W. Hewak, and C. Soci, *Sci. Rep.* **6**, 35409 (2016).
- ¹⁰H. W. Lee, M. A. Schmidt, R. F. Russell, N. Y. Joly, H. K. Tyagi, P. Uebel, and P. S. J. Russell, *Opt. Express* **19**(13), 12180 (2011).
- ¹¹H. Zhang, N. Healy, L. Shen, C. C. Huang, D. W. Hewak, and A. C. Peacock, *Sci. Rep.* **6**(1), 23512 (2016).
- ¹²Q. Bao, H. Zhang, B. Wang, Z. Ni, C. H. Y. X. Lim, Y. Wang, D. Y. Tang, and K. P. Loh, *Nat. Photonics* **5**(7), 411–415 (2011).
- ¹³A. Xomalis, I. Demirtzioglou, E. Plum, Y. Jung, V. Nalla, C. Lacava, K. F. MacDonald, P. Petropoulos, D. J. Richardson, and N. I. Zheludev, *Nat. Commun.* **9**(1), 182 (2018).
- ¹⁴M. A. Caldwell, S. Raoux, R. Y. Wang, H. S. Philip Wong, and D. J. Milliron, *J. Mater. Chem.* **20**(7), 1285–1291 (2010).
- ¹⁵C.-C. Huang, F. Al-Saab, Y. Wang, J.-Y. Ou, J. C. Walker, S. Wang, B. Gholipour, R. E. Simpson, and D. W. Hewak, *Nanoscale* **6**(21), 12792–12797 (2014).
- ¹⁶B. J. Eggleton, B. Luther-Davies, and K. Richardson, *Nat. Photonics* **5**(3), 141–148 (2011).
- ¹⁷G. Tao, H. Ebendorff-Heidepriem, A. M. Stolyarov, S. Danto, J. V. Badding, Y. Fink, J. Ballato, and A. F. Abouraddy, *Adv. Opt. Photonics* **7**(2), 379 (2015).
- ¹⁸S. Guerin, B. Hayden, D. W. Hewak, and C. Vian, *ACS Comb. Sci.* **19**(7), 478–491 (2017).
- ¹⁹A. Zakery and S. R. Elliott, *J. Non-Cryst. Solids* **330**(1-3), 1–12 (2003).
- ²⁰K. S. Bindra, H. T. Bookey, A. K. Kar, B. S. Wherrett, X. Liu, and A. Jha, *Appl. Phys. Lett.* **79**(13), 1939–1941 (2001).
- ²¹V. Ta'eed, N. J. Baker, L. Fu, K. Finsterbusch, M. R. E. Lamont, D. J. Moss, H. C. Nguyen, B. J. Eggleton, D.-Y. Choi, S. Madden, and B. Luther-Davies, *Opt. Express* **15**(15), 9205 (2007).
- ²²D. Piccinotti, B. Gholipour, J. Yao, K. F. Macdonald, B. E. Hayden, and N. I. Zheludev, *Opt. Express* **26**(16), 20861 (2018).
- ²³W. S. Whitney, V. W. Brar, Y. Ou, Y. Shao, A. R. Davoyan, D. N. Basov, K. He, Q.-K. Xue, and H. A. Atwater, *Nano Lett.* **17**(1), 255–260 (2016).
- ²⁴B. Gholipour, D. Piccinotti, A. Karvounis, K. F. MacDonald, and N. I. Zheludev, *Nano Lett.* **19**, 1643 (2019).
- ²⁵J. Yin, H. N. S. Krishnamoorthy, G. Adamo, A. M. Dubrovkin, Y. Chong, N. I. Zheludev, and C. Soci, *NPG Asia Mater.* **9**(8), e425 (2017).
- ²⁶D. Piccinotti, B. Gholipour, J. Yao, K. F. MacDonald, B. E. Hayden, and N. I. Zheludev, *Adv. Mater.* **31**, 1807083 (2019).
- ²⁷M. I. Stockman, K. Kneipp, S. I. Bozhevolnyi, S. Saha, A. Dutta, J. Ndukaife, N. Kinsey, H. Reddy, U. Guler, V. M. Shalae, A. Boltasseva, B. Gholipour, H. N. S. Krishnamoorthy, K. F. MacDonald, C. Soci, N. I. Zheludev, V. Savinov, R. Singh, P. Grof, C. Lienau, M. Vadai, M. L. Solomon, D. R. Barton, M. Lawrence, J. A. Dionne, S. V. Boriskina, R. Esteban, J. Aizpurua, X. Zhang, S. Yang, D. Wang, W. Wang, T. W. Odom, N. Accanto, P. M. de Roque, I. M. Hancu, L. Piatkowski, N. F. van Hulst, and M. F. Kling, *J. Opt.* **20**(4), 043001 (2018).
- ²⁸B. Gholipour, A. Karvounis, J. Yin, C. Soci, K. F. MacDonald, and N. I. Zheludev, *NPG Asia Materials* **10**, 533 (2018).
- ²⁹D. Piccinotti, B. Gholipour, J. Yao, K. F. MacDonald, B. E. Hayden, and N. I. Zheludev, *Adv. Opt. Mater.* **6**(22), 1800395 (2018).
- ³⁰K. B. Borisenko, J. Shanmugam, B. A. O. Williams, P. Ewart, B. Gholipour, D. W. Hewak, R. Hussain, T. Javorfi, G. Siligardi, and A. I. Kirkland, *Sci. Rep.* **5**, 8770 (2015).
- ³¹L. B. Shaw, B. Cole, P. A. Thielen, J. S. Sanghera, and I. D. Aggarwal, *IEEE J. Quantum Electron.* **37**(9), 1127–1137 (2001).
- ³²M. A. Hughes, R. M. Gwilliam, K. Homewood, B. Gholipour, D. W. Hewak, T.-H. Lee, S. R. Elliott, T. Suzuki, Y. Ohishi, T. Kohoutek, and R. J. Curry, *Opt. Express* **21**(7), 8101 (2013).
- ³³C. C. Huang, B. Gholipour, J. Y. Ou, K. Knight, and D. W. Hewak, *Electron. Lett.* **47**(4), 288 (2011).
- ³⁴M. Wuttig and N. Yamada, *Nat. Mater.* **6**(12), 1004 (2007).
- ³⁵S. R. Ovshinsky, *Phys. Rev. Lett.* **21**(20), 1450–1453 (1968).
- ³⁶D. Loke, T. H. Lee, W. J. Wang, L. P. Shi, R. Zhao, Y. C. Yeo, T. C. Chong, and S. R. Elliott, *Science* **336**(6088), 1566–1569 (2012).
- ³⁷D. Kuzum, R. G. D. Jeyasingh, B. Lee, and H. S. P. Wong, *Nano Lett.* **12**(5), 2179–2186 (2012).
- ³⁸C. Ríos, M. Stegmaier, P. Hosseini, D. Wang, T. Scherer, C. D. Wright, H. Bhaskaran, and W. H. P. Pernice, *Nat. Photonics* **9**, 725 (2015).
- ³⁹Q. Wang, E. T. F. Rogers, B. Gholipour, C.-M. Wang, G. Yuan, J. Teng, and N. I. Zheludev, *Nat. Photonics* **10**(1), 60–65 (2015).
- ⁴⁰G. T. Reed, G. Mashanovich, F. Y. Gardes, and D. J. Thomson, *Nat. Photonics* **4**(9), 660 (2010).
- ⁴¹S. Vasil'ev, O. Medvedkov, I. Korolev, A. Bozhkov, A. Kurkov, and E. Dianov, *Quantum Electron.* **35**(12), 1085 (2005).
- ⁴²T. Erdogan, *J. Opt. Soc. Am. A* **14**(8), 1760 (1997).